Please cite the Published Version

Additional Information: This is an open access article published in Technologies, by MDPI.

Data Access Statement: Data are available upon request to the corresponding author.

Article

Design of Multi-Sourced MIMO Multiband Hybrid Wireless RF-Perovskite Photovoltaic Energy Harvesting Subsystems for Iots Applications in Smart Cities

Fanuel Elias [1,†] , Sunday Ekpo [1,*,†] , Stephen Alabi [2], Mfonobong Uko [1,†] , Sunday Enahoro [1] , Muhammad Ijaz [1] , Helen Ji [1], Rahul Unnikrishnan [1,2,†] and Nurudeen Olasunkanmi [2]

[1] Communication and Space Systems Engineering Research Team, Manchester Metropolitan University, Manchester M1 5GD, UK; fanuel.elias@stu.mmu.ac.uk (F.E.); mfonobong.uko@stu.mmu.ac.uk (M.U.); sunday.enahoro@stu.mmu.ac.uk (S.E.); m.ijaz@mmu.ac.uk (M.I.); h.ji@mmu.ac.uk (H.J.); rahul.unnikrishnan@mmu.ac.uk (R.U.)
[2] SmOp Cleantech, Wilsons Park, Monsall Road, Manchester M40 8WN, UK; stephen.alabi@smopct.com (S.A.); kolawole@smopct.com (N.O.)
* Correspondence: s.ekpo@mmu.ac.uk
† These authors contributed equally to this work.

Abstract: Energy harvesting technology allows Internet of Things (IoT) devices to be powered continuously without needing battery charging or replacement. In addressing existing and emerging massive IoT energy supply challenges, this paper presents the design of multi-sourced multiple input and multiple output (MIMO) multiband hybrid wireless RF-perovskite photovoltaic energy harvesting subsystems for IoT application. The research findings evaluate the efficiency and power output of different RF configurations (1 to 16 antennas) within MIMO RF subsystems. A Delon quadruple rectifier in the RF energy harvesting system demonstrates a system-level power conversion efficiency of 51%. The research also explores the I-V and P-V characteristics of the adopted perovskite tandem cell. This results in an impressive array capable of producing 6.4 V and generating a maximum power of 650 mW. For the first time, the combined mathematical modelling of the system architecture is presented. The achieved efficiency of the combined system is 90% (for 8 MIMO) and 98% (for 16 MIMO) at 0 dBm input RF power. This novel study holds great promise for next-generation 5G/6G smart IoT passive electronics. Additionally, it establishes the hybrid RF-perovskite energy harvester as a promising, compact, and eco-friendly solution for efficiently powering IoT devices in smart cities. This work contributes to the development of sustainable, scalable, and smart energy solutions for IoT integration into smart city infrastructures.

Keywords: energy harvesting; hybrid; Internet of things; MIMO; perovskite photovoltaic; smart cities; wireless RF

1. Introduction

Today, sustainability is a major global issue, worsened by the increasing use of fossil fuels. The necessity for sustainable and efficient energy sources has become increasingly important with the rapidly evolving landscape of IoT applications. As a result, smart energy and carbon-free energy generation methods, such as energy harvesting from environmental sources like wind, solar, and electromagnetic waves, are emerging as key enablers for IoT devices [1] and the expansion of smart cities. These smart cities rely heavily on smart energy, smart sensing, and resilient infrastructure to support their interconnected systems.

As shown in Figure 1, common energy harvesting technologies include solar, thermal, vibrational, and RF harvesters. Each is designed for specific environments, contributing to improved sustainability in IoT ecosystems with unique capabilities [2]. IoT devices have transformed numerous sectors, such as healthcare, agriculture, manufacturing, and smart cities [3]. With the growing number of IoT devices, RF waves are rising in the environment. Hence, an efficient method is required to extract energy from the available spectrum and power IoT devices [4,5].
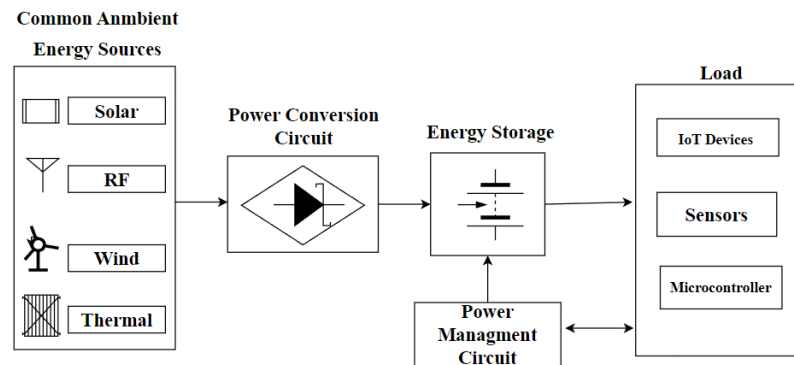
Figure 1. Common types of ambient energy harvesting.

The emergence of 5G/6G satellite–cellular networks with terrestrial and non-terrestrial networks (NTNs) promises seamless, ubiquitous communication capabilities [6–10]. The convergence of 5G/6G/Wi-Fi 6/6E/7 will enhance massive IoT device deployments at an unprecedented rate [11–15]. Future IoT technologies in smart cities and heterogeneous TN-NTN ecosystems will require energy efficiency, spectrum efficiency, and reconfigurable signal coverage across various network ranges, from the wireless personal area network (WPAN) (10–100 m) to the wireless vast area network (WWAN) (up to 100 km) [15–17]. Wi-Fi 6/6E, with its additional 6-GHz band, boosts data rates to 9607 Mb/s, surpassing Wi-Fi 5's 3476 Mb/s by using 1024-QAM OFDMA and uplink/downlink MU-MIMO (UL/DL MU-MIMO), enabling massive IoT growth. As 5G/6G networks continue to evolve with high speed, low latency, and increased bandwidth, the demand for wireless power transfer (WPT) and energy harvesting solutions will grow [18], offering a practical means to sustain the massive deployment of IoT devices in smart cities.

Integrating energy harvesting technologies with modern wireless communication networks offers a sustainable power solution for IoT devices, especially in smart cities and remote areas [6]. Since the 1990s, RF energy harvesting has become more feasible due to the widespread use of TV, radio, cellular, satellite, and Wi-Fi signals, which create ambient RF energy [19,20]. This energy is captured and converted into usable electrical power by a rectifier and regulated by a power management unit [21,22], a typical RF energy harvesting block diagram is given in Figure 2. While RF energy harvesting alone may not always meet the full energy demands of IoT devices, the adaptability and versatility of these solutions mean that they can be combined with other technologies, like perovskite photovoltaic cells, to provide sufficient power for ultra-low-powered IoT applications, such as security surveillance and smart sensing in smart buildings, smart infrastructures, and intelligent agriculture [22,23].
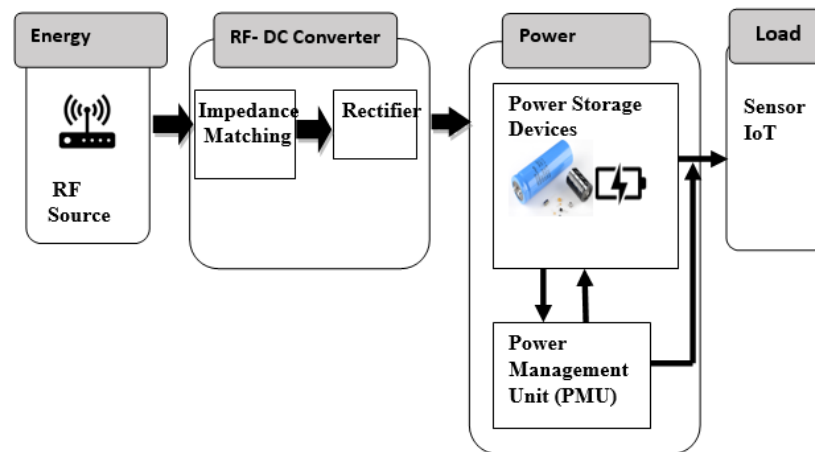
Figure 2. RF energy harvesting block diagram.

Perovskite solar cells (PSCs) are highly efficient solar cells made from a perovskite-structured compound, typically a hybrid organic–inorganic material containing lead or tin halide. Over the past five years, PSCs have surpassed most thin-film technologies in power conversion efficiency, maintaining a consistently high efficiency even in low-intensity or diffuse light [22]. These attributes make them ideal for hybrid energy harvesting applications, including indoor and outdoor environments [24]. A recent technological breakthrough has facilitated the development of hybrid energy harvesting systems by evaluating the features and trade-offs linked to these harvesters. These hybrid designs can integrate many energy sources and efficiently substitute batteries in IoT applications, relieving technicians from the need to replace batteries often and expensively [25]. The subsystem is designed to efficiently gather and convert many energy sources into usable electrical energy [26].

This study explores MIMO technology in energy harvesting, emphasising using multiple antennas for enhanced output voltage and efficiency, spatial multiplexing, filtering, and diversity [27,28]. It introduces a novel approach by integrating MIMO RF-EH with PSCs, addressing the challenges of low output voltage. The proposed energy harvesting system, Figure 3, combines MIMO with multiple energy sources across different frequency bands, improving IoT capabilities and reducing dependence on traditional energy sources. This hybrid wireless RF-perovskite system ensures reliable, continuous power and offers lower maintenance costs and deployment flexibility. It is well-suited for IoT applications such as environmental monitoring, wearables, and intelligent infrastructure. Additionally, it provides a sustainable IoT power solution using a hybrid multi-radio frequency system and cost-effective thin-film solar cells optimised for indoor use [22] in smart cities.
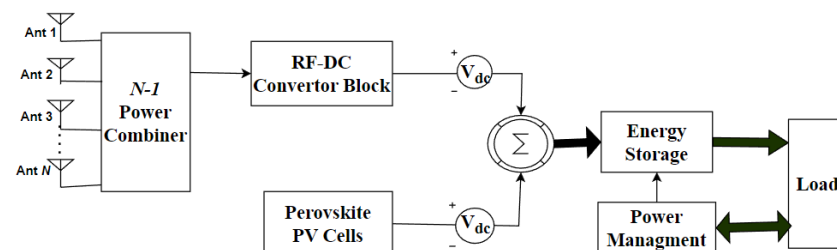
Figure 3. Proposed RF−perovskite multi-source energy harvesting block diagram.

2. Overview of MIMO Technology and Multi-band Systems

MIMO technology is pivotal for optimising energy harvesting in IoT systems by enabling the simultaneous transmission and reception of multiple signals, which boosts

energy transfer efficiency. It enables efficient power transmission from RF sources [23] and ensures energy balance across network components by allowing each node to function as a transmitter and relay [29]. Through MIMO technology, Figure 4, IoT devices can efficiently harvest energy from multiple RF sources concurrently, resulting in improved energy efficiency and harvesting capabilities [25]. MIMO's resilience to noise and jitter ensures consistent energy transmission, which is vital for various IoT applications [10]. Additionally, it enhances overall system performance by facilitating directional energy transmission through beam-forming, making it ideal for multi-sourced MIMO multi-band hybrid RF-perovskite photovoltaic energy harvesting subsystems, thereby improving IoT device power supply capabilities in smart cities [6,29].

Simultaneous wireless information and power transfer (SWIPT) technology ensures reliable and uninterrupted energy acquisition. To enhance the SWIPT system's energy efficiency, a complex physical layer technique considering data transmission rate and energy harvesting performance is crucial [30]. Two user grouping techniques and a dynamic power allocation solution were suggested for a multi-input, multi-output, non-orthogonal multiple access (MIMO-NOMA) system to optimise energy harvesting by including SWIPT. These techniques achieved maximum energy and information transmission using RF signals [31]. Multi-band technology enables system operation across various frequency bands, providing flexibility in capturing RF energy from diverse sources. This approach ensures that the IoT device can extract energy from various RF signals, optimise energy harvesting capacity, and enhance overall power output. The proposed design combines a PSCs array with RF energy harvesting subsystems, utilising abundant sunlight and RF waves from communication systems to build a multi-sourced MIMO hybrid system that efficiently powers IoT devices and supports future IoT paradigms.
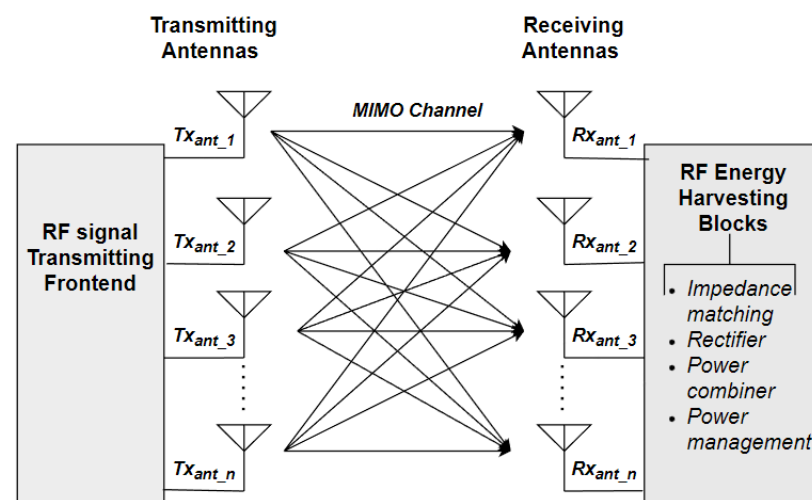
Figure 4. MIMO system in RF energy harvesting.

3. Perovskite Photovoltaic: Basics and Related Work

Solar power is a vital renewable energy solution for meeting global energy demands. Solar panels, also called photovoltaics (PVs), convert sunlight into electricity and are critical for solar energy systems. These cells typically generate an open circuit voltage (V_{oc}) over 0.9 V under artificial sunlight (AM 1.5) or visible light [32]. The main PV types are monocrystalline, polycrystalline, thin-film, and perovskite. Monocrystalline cells offer higher efficiency but are more expensive, while polycrystalline options are more affordable for large-scale use but less efficient. A monocrystalline silicon cell with an n-type structure has achieved a 21.3% conversion efficiency using a passivated emitter and rear-diffused design [33].

Silicon (Si) solar cells dominate the current PV market, with a theoretical efficiency limit of around 29.4% for single-junction cells. Multi-junction structures using absorbers with suitable bandgaps have been developed to enhance efficiency and reduce thermalisation losses [34]. Tandem configurations of III-V materials with Si have achieved efficiencies over 32% [35,36], but their high cost limits widespread adoption. Consequently, organic–inorganic metal halide lead PSCs have gained attention for their impressive 25.2% efficiency [37]. Despite facing durability and stability challenges, PSCs offer comparable efficiency to Si cells at a lower production cost, enhancing their appeal as alternatives in the PV market [38].

Researchers are drawn to perovskite materials for their unique crystal structure, offering excellent light absorption, performance, low-temperature processability, and versatility as light energy harvesters [39]. PSCs utilise perovskites with an ABX_3 crystal structure. In this structure, organic cations (methylammonium or formamidinium) or inorganic cations (Cs^+ and Rb^+) serve as A cations. B cations are divalent ions (Pb^{2+}, Sn^{2+}, or Ge^{2+}), while X represents halide anions (I^-, Cl^-, or Br^-) [40]. Two typical designs are employed in PSC-Si tandem solar cells (Figure 5): mechanically or optically stacked four-terminal (4T) and monolithically integrated two-terminal (2T) architectures. In 2T tandems, high-bandgap perovskite cells are stacked directly on silicon cells, requiring precise current matching due to their electrical series connection. Conversely, 4T tandems involve separate production of the two cells, which are then connected at the module level using optical coupling, which eases current matching but increases production complexity. Both configurations require a semitransparent upper cell with minimal parasitic absorption [34].
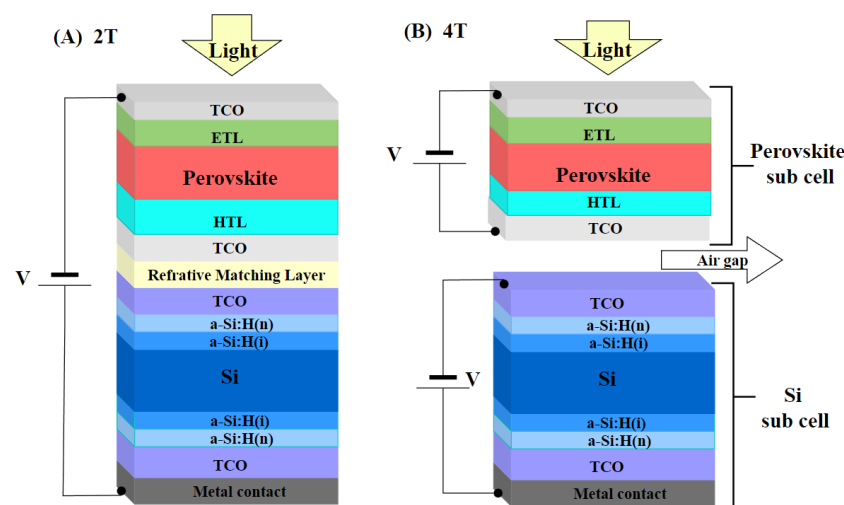
Figure 5. Schematic diagram of common PSC architectures: 2-terminal (**A**) and 4-terminal (**B**).

Recent advances in 2T and 4T perovskite–Si tandem cells have achieved power conversion efficiencies (PCEs) of 28.27% [41] and 31.34% [42], respectively. However, these configurations face current and spectrum matching challenges, resulting in lower short-circuit current density (J_{sc}) in bottom Si cells, typically ranging from 14 to 19 mA/cm², significantly lower than the original Si cells, which had a J_{sc} of approximately 40 mA/cm². Consequently, half of the output power would be lost [42]. Single-junction PSCs show strong efficiency, but semitransparent versions are less efficient due to difficulties in applying transparent electrodes without damaging underlying layers [43,44]. Moreover, single-junction PSCs reached 38.18% efficiency under Sun conditions and 13.18% under light emitting diode's (LED) light [45], while concentrated PV cells can exceed 40% under optimal conditions, making them suitable for regions with ample direct sunlight, surpassing the Shockley–Queisser limit of 33% [45].

The study in [39] introduced a cost-effective indoor sensing method using PSCs for powering backscatter sensors. Additionally, [32] generated about 1 V photovoltage using a red LED, while [46] developed a wireless temperature sensor powered by PSCs, offering a 4 m communication range and 4.3 V output. These prototypes highlight the potential of PSCs to meet the energy demands of IoT devices, though efficiency enhancements are necessary.

4. System Architecture and Design Procedures

4.1. RF Energy Harvesting System

A typical RF energy harvesting (RF-EH) system, as shown in Figure 2, consists of crucial components for capturing, converting, and managing ambient RF energy. The system includes an antenna strategically placed to capture ambient RF energy, directing the received power to a rectifier circuit [7]. The rectifier plays a vital role by converting RF power into DC power, which is then stored or managed in a system using capacitors or batteries for future use [47]. Impedance matching connects the antenna and the rectifier and is vital to reduce signal loss and ensure efficient energy transfer, especially with low-input RF signals. A high-quality matching network and low-loss rectifier are critical for optimising power transfer and system performance [48].

This paper presents the design and simulation of an RF-EH system using Keysight Advanced Design System (ADS) 2023 update 1.0 software, developed by Keysight Technologies, headquartered in Santa Rosa, CA, USA. A variable RF power source ($P1_T one$) with input power ranging from -25 to 20 dBm was used as the antenna input to evaluate system performance across different power levels. The simulation was conducted at 2.4 GHz, targeting indoor IoT applications, commonly using WIFI-4 and WIFI-6. The rectifier generates an output voltage (V_{dc}) and current (I_o) at a fixed load, as shown in Figure 6, with V_{dc} exhibiting minimal ripple, stabilised by a 470 pF capacitor.
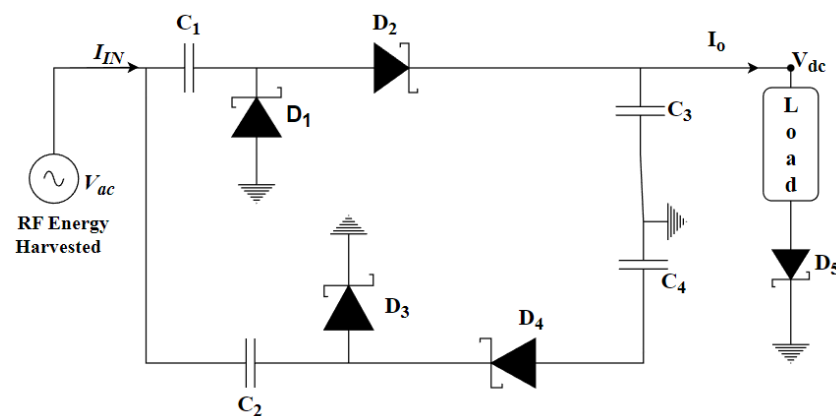
Figure 6. Delon quadruple rectifier used in the RF energy harvester.

A RF-EH system at low power levels, often as low as -25 dBm (3.2 μW), poses significant challenges due to the high threshold voltages of conventional diodes [47,49]. For a typical 50 Ohm antenna, the resulting peak AC voltage may be as low as 5.7 mV, necessitating diodes with low forward voltage drop (V_f) and fast switching speeds to ensure efficient rectification [18,47]. Schottky diodes, such as the SMS7630 (Skyworks, V_f = 150–250 mV and HSMS-2860 (Broadcom, V_f = 150 mV), are well-suited for these applications due to their low conduction threshold and high-frequency operation. Forward voltage drops and reverse leakage current impact overall rectification efficiency and result in power dissipation in Schottky diodes. Impedance matching networks are employed to optimise power transfer and reduce reflection losses. Multi-stage rectifiers, including

voltage multipliers (such as the Delon quadruple rectifier), help compensate for low RF voltage levels, improving DC output without significantly increasing power dissipation. Advanced semiconductor materials, such as graphene-based and tunnel diodes, further enhance energy conversion efficiency with even lower voltage drops and faster response times. Effective thermal management techniques, such as heat sinks and PCB thermal vias, prevent overheating and maintain performance stability [12]. This study selected the HSMS-2860 Schottky diode due to its wide operating frequency range (up to 24 GHz), low turn-on voltage, and market availability. By integrating optimised rectification techniques, low-V_f Schottky diodes, and advanced power management strategies, RF energy harvesting systems can achieve higher efficiency, making them viable for low-power IoT and wireless sensor applications [49].

The RF Schottky diode HSMS-2860 was used in this research due to its low forward voltage drop and high switching speed, which make it ideal for rectification. A unique Delon quadruple rectifier (Figure 6), known for its high RF-DC conversion efficiency, was implemented in the RF-EH system to boost voltage conversion and significantly enhance system performance. The rectifier was designed and simulated using ADS software, and its efficiency was calculated using (5). A diode was added in series with the load resistance to improve sensitivity, allowing the RF-EH system to operate effectively down to −25 dBm. The Schottky diode's current–voltage relationship (1) describes the current flowing through the diode (I_D) to the applied voltage (V_D). Understanding this behaviour is fundamental for effective rectification. The diode voltage, V_D, is provided in (2).

$$I_D = I_s \cdot (e^{(V_D/\eta \cdot V_T)} - 1), \tag{1}$$

$$V_D = \eta \cdot V_T \cdot ln((\frac{I_o}{I_s}) + 1), \tag{2}$$

where the reverse saturation current is (I_s), η is the ideality factor, i.e., the deviation of an actual diode's behaviour from the ideal diode model, and V_T is thermal voltage provided by kT/q.

The input RF signal to the rectifier, represented as V_{ac}, varies with frequency. The average output current of the rectifier, I_o, can be expressed using (3).

$$I_o = \frac{1}{T} \cdot \int_0^T I_D \cdot dt. \tag{3}$$

The output current, I_o, can be analysed for two key energy harvesting scenarios: optimising device efficiency and maximising energy storage [48]. The maximum energy storage of the system occurs at the no-load output voltage, $I_o = 0$, which is determined by (4).

$$E_{RF} = \frac{(C_{out} \cdot V_{dc}^2)}{2}. \tag{4}$$

The proposed rectifier functions during a complete cycle, transferring an average power ($V_{ac} \cdot I_{IN}$) from the RF source. The maximum power available to the rectifier is ($V_{ac} \cdot I_{IN})/2$ when optimal impedance matching is applied. The corresponding PCE of the rectifier is defined as the ratio of input RF power (P_{IN}) to output DC power (P_O) and is provided by (5).

$$PCE = \frac{P_O}{P_{IN}}, \tag{5}$$

where

$$P_{IN} = \frac{V_{ac} \cdot I_{IN}}{2} \quad and \quad P_O = \frac{V_{dc}^2}{R_L}. \tag{6}$$

The efficiency of an RF-EH system relies on the antenna's performance, impedance matching, and rectifier efficiency. Thus, the energy harvesting efficiency of a single-input single-output (SISO) RF-EH system (η_{SISO}) is defined by (7).

$$\eta_{SISO} = (PEE_{ant} \times PCE_{MN} \times PCE),\qquad(7)$$

where,

$$PEE_{ant} = \frac{P_{input.MN}}{P_{received.antenna}} \quad and \quad PCE_{MN} = \frac{P_{input.rectifier}}{P_{input.MN}}.\qquad(8)$$

The PCE of the rectifier is provided in (5). The power extraction efficiency of the receiving antenna PEE_{ant} and the power conversion efficiency of the impedance matching network PCE_{MN} can be calculated using (8).

MIMO configurations in RF-EH provide benefits like spatial diversity, adaptability to varying environments, increased robustness, and potentially greater efficiency compared to standard antenna arrays [50]. This investigation evaluates MIMO technology by employing multiple RF power sources as antennas, focusing on configurations with 1, 2, 4, 8, and 16 antennas for IoT applications. Each MIMO subsystem comprises an SISO RF-EH setup, including an antenna, matching network, and rectifier, with their output powers combined using a power combiner tool in ADS. Efficiency is assessed using probability theory, with each subsystem's efficiency, η_{SISO}, representing the probability of successful energy harvesting. The overall MIMO RF-EH efficiency, η_{RF}, is determined as one minus the product of the complementary probabilities $(1 - \eta_{SISO})$.

$$\eta_{RF} = 1 - \prod_{N=1}^{2^a} (1 - (\eta_{SISO})_N).\qquad(9)$$

In this context, $(\eta_{SISO})_N$ represents the efficiency of the N-th antenna in the RF-EH system. The variable N ranges from 1 to 2^a, where a varies from 0 to 4, corresponding to MIMO RF-EH with 1, 2, 4, 8, and 16 antennas, respectively.

Several optimisation techniques can be implemented on the antenna front-end of the RF energy harvesting subsystems to further enhance the performance of the MIMO RF energy harvesting system. The integration of adaptive impedance matching networks ensures that the impedance of the rectifier and the antenna remains optimally aligned across varying RF input conditions. Moreover, reconfigurable metasurface-based antenna designs enhance wavefront manipulation, optimising RF energy absorption and redistribution within the MIMO systems. By integrating beam-forming techniques, RF energy can be dynamically focused toward the energy harvesting antenna at higher power densities, maximising received power while reducing interference. High-gain configurations, such as MIMO arrays, metasurfaces, and fractal geometries, improve RF energy capture and directivity while using low-loss substrates and metamaterials to improve radiation efficiency. A critical component for optimised RF energy harvesting is a high-PCE, low-power rectifier architecture, especially under low RF input power conditions. This study employs such a rectifier to improve power output and efficiency.

4.2. Perovskite Photovoltaic Energy Harvesting System

Significant research has focused on enhancing the performance and efficiency of PV energy harvesting cells, particularly PSCs, which have made remarkable strides over the past decade, achieving efficiencies between 5% and 33% [51,52]. The PV characteristics, represented by I-V and P-V curves, are essential for optimising system performance and assessing the efficiency and reliability of solar energy conversion. While PSCs and Si cells show minor differences in hysteresis and temperature sensitivity, both aim to convert sun-

light into electricity, possess a maximum power point, and focus on efficiency optimisation. These characteristic curves can be generated using single or double-diode modelling, with the latter being more complex to develop and implement [53].

This section presents the mathematical modelling of PV systems, both cell and module, utilising the one-diode model. The equivalent circuit model for the cell, as shown in Figure 7, includes components such as a photocurrent (I_{ph}), diode ($D1$), series resistor (R_s), and shunt resistor (R_{sh}). R_s represents the resistance in the current circuit, primarily caused by losses from metal grids, semiconductor materials, and interconnections. At the same time, R_{sh} is associated with current leakage due to cell thickness and surface effects. The impact of R_s is more pronounced at the cell level due to the multiplication of resistances within a module, whereas R_{sh} becomes significant when multiple PV modules are involved [54]. Figure 7 illustrates the cell's V_{out} and I_{ph}, which are directly proportional to incident light on the cell and expressed in (10).
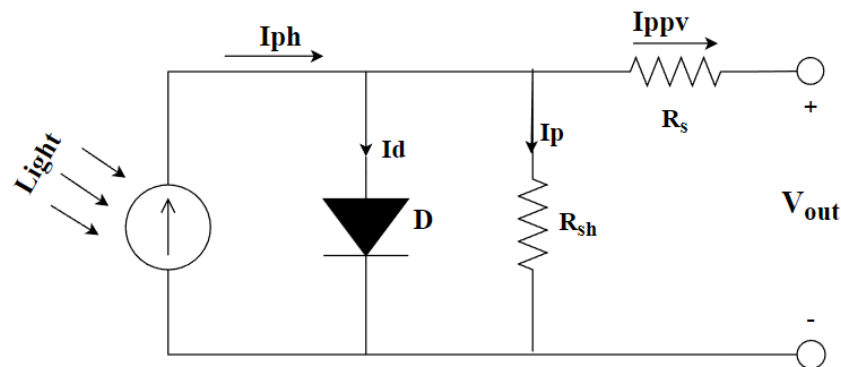

Figure 7. Single−diode PV cell equivalent circuit.

$$I_{ph} = [I_{sc} + K_i(T_o - T_s)] \times \frac{G}{1000},$$ (10)

where irradiance (G) is 1000 W/m^2 in standard test conditions (STC), I_{sc} is the short-circuit current at STC, K_i is temperature coefficient of I_{sc}, T_o is cell temperature, and T_s is standard temperature (298 K).

The reverse saturation current for a single PSCs, $I_{s,r}$, is as follows:

$$I_{s,r} = \frac{I_{sc}}{e^{\left(\frac{q \times V_{oc}}{k \times A \times T_o}\right)} - 1}.$$ (11)

Referring to Figure 7, the expressions for the current through the diode (D), (I_d), the current through R_{sh}, I_p, the output current (I_{ppv}), and the output power (P_{ppv}) of a PV cell at a load (R_L) are as follows:

$$I_d = I_s[e^{\left(\frac{V_{out} + I_{ppv} \times R_s}{A \times V_T}\right)} - 1],$$ (12)

$$I_p = \frac{V_{out} + I_{ppv} \times R_s}{R_{sh}},$$ (13)

$$I_{ppv} = I_{ph} - I_d - I_p,$$ (14)

$$P_{ppv} = \frac{I_{ppv}^2}{R_L}.$$ (15)

In (10) and (11), V_T is the thermal voltage equivalent (V), $V_T = \frac{k \times T_o}{q}$, q is electron charge (1.6×10^{-19} C), V_{oc} is the open circuit voltage, k represents the Boltzmann constant (1.3806×10^{-23} J/K), and A is the ideality factor for PSCs.

A single PSC produces low output power, but its voltage or current can be increased to meet IoT device requirements by combining multiple PSCs. This can be carried out by connecting cells in a series to form a perovskite module or by creating a perovskite array by connecting modules in parallel. The performance of these configurations can be assessed by calculating the voltage from a single cell multiplied by the number of series-connected cells for module voltage and the current multiplied by the number of parallel-connected cells or modules for the array current. The configuration of the general PSCs, shown in Figure 8, varies based on the number of series diodes (Y_s) and parallel diodes (X_p). A PSC is represented as ($X_p = Y_s = 1$), a module as ($X_p = 1, Y_s \neq 1$), and an array as ($X_p = Y_s \neq 1$). Equation (11) can be modified for the perovskite module reverse saturation current, $I_{s,r,M}$, as follows:

$$I_{s,r,M} = \frac{I_{sc}}{e^{\left(\frac{q \times V_{oc}}{Y_{sc} \times k \times A \times T_o}\right)} - 1}. \tag{16}$$

The photon currents of the modules (I_{ph1}, I_{ph2}, . . . $I_{ph_{X_p}}$) (Figure 6) are identical and equal to the incident light on the unit PSCs (I_{ph}), as outlined in (10). Hence, ($I_{ph_1} = I_{ph_2} = \ldots = I_{ph_{(X_p-1)}} = I_{ph_{X_p}} = I_{ph}$). Thus, the perovskite array incident current, I_{PH}, is expressed by (17) or (18).

$$I_{PH} = X_p \times I_{ph}, \tag{17}$$

$$I_{PH} = \sum_{k=1}^{X_p} I_{ph_k}. \tag{18}$$

The perovskite array's output current (I_{PSCs}), illustrated in Figure 8, is expressed as follows:

$$I_{PSCs} = I_{PH} - (X_p \times I_d) - I_P. \tag{19}$$

Hence, the current (I_P) through R_{sh} is defined by (20).

$$I_P = \frac{(V_{PSCs} \times X_p/Y_S) + (I_{PSCs} \times R_s)}{R_{sh}}. \tag{20}$$

Hence, the output current for a PSC array, depicted in Figure 8, composed of Y_s cells connected in series and X_p modules in parallel, can be mathematically expressed as follows:

$$I_{PSCs} = \sum_{k=1}^{X_p} I_{ph_k} - X_p \cdot I_s\left(e^{\left(\frac{\frac{V_{PSCs}}{Y_s} + \frac{I_{PSCs} \cdot R_s}{X_p}}{A \cdot V_T}\right)} - 1\right) - I_P. \tag{21}$$
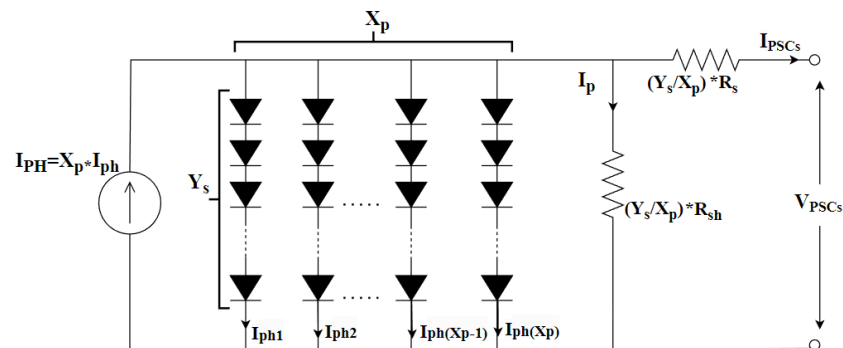

Figure 8. PSC array equivalent circuit.

In general, Equations (17), (19) and (20) can be adapted for unit cells by setting $X_p = Y_s = 1$ and for modules by setting $X_p = 1$ and $Y_s \neq 1$. The power generated by PSCs, P_{PSCs}, supplies energy to IoT devices during the operational time (t_{PSCs}), which is

the maximum available time (t_m) minus the inactive duration (t_{off}) when the cell cannot produce electricity due to low light or shading. The electric power (P_{PSCs}) and total harvested energy (E_{PSCs}) from a perovskite array can be computed as follows:

$$P_{PSCs} = \frac{I_{PSCs}^2}{R_L}, \tag{22}$$

$$E_{PSCs} = P_{PSCs} \times t_{PSCs} = P_{PSCs}(t_m - t_{off}). \tag{23}$$

The efficiency of a cell, η_c, is determined using (24), considering key parameters such as open circuit voltage (Voc), short circuit current (I_{sc}), input irradiation power (P_{in}), fill factor (FF_{cell}), and the current (I_{mp}) and voltage (V_{mp}) at the maximum power point (MPP).

$$\eta_c = \frac{FF_{cell} \times V_{oc} \times I_{sc}}{P_{in}} \tag{24}$$

$$FF_{cell} = \frac{I_{mp} \times V_{mp}}{I_{sc} \times V_{oc}}. \tag{25}$$

Substituting the expression (25), FF_{cell}, into (24) gives:

$$\eta_c = \frac{I_{mp} \times V_{mp}}{P_{in}}. \tag{26}$$

The efficiency of a PSC array is evaluated using (9), which factors in the efficiencies of individual modules arranged in parallel. Each module's efficiency is determined by multiplying the series-connected cells' efficiencies. The module's efficiency, η_M, is provided by (27).

$$\eta_M = \eta_{c1} \times \eta_{c2} \times \eta_{c3} \times \cdots \eta_{Y_s}. \tag{27}$$

In this context, $\eta_{c1}, \eta_{c2}, \eta_{c3}, \ldots, \eta Y_s$ represent the efficiencies of individual PSCs within the module. Since these cells are identical and made from the same material, their efficiencies are equal and denoted as η_c. Therefore, (27) can be simplified as follows:

$$\eta_M = (\eta_c)^{Y_s}. \tag{28}$$

The overall efficiency of the entire PSCs system array, η_A, is as follows:

$$\eta_A = 1 - \prod_{N=1}^{X_P} (1 - (\eta_M)_N), \tag{29}$$

where N represents the number of parallel-connected modules, ranging from 1 to X_P (Figure 8). Since all the modules have equal efficiency, (29) can be simplified as follows:

$$\eta_A = 1 - [1 - (\eta_M)]^{X_P}. \tag{30}$$

This study utilises data from a previously reported perovskite-on-Si tandem solar cell [55] for mathematical analysis and assessment of PSCs. I-V and P-V curves are generated and depicted using MATLAB (version 9.9) in Figure 9. The ADS software is employed to develop and simulate a diode model, shown in Figure 7, to replicate the PV characteristics illustrated in Figure 9. Within the ADS simulation, a current source represents the photon current generated by the cell due to irradiation. Individual cells demonstrate I_{mp}, V_{mp}, and P_{max} values of 21.69 mA, 1.99 V, and 43.36 mW, respectively, as depicted in Figure 9. Cells are arranged in series and parallel to meet the power requirements of IoT devices, with results detailed in the next section. Like other solar systems, the perovskite-on-Si tandem solar array stops operating during darkness or at night due to decreased photon

current, making the cell inactive as it functions like a diode, producing no voltage or current. Therefore, an alternative energy source is necessary to power IoT devices overnight, leading to the proposal of a hybrid energy harvesting system.
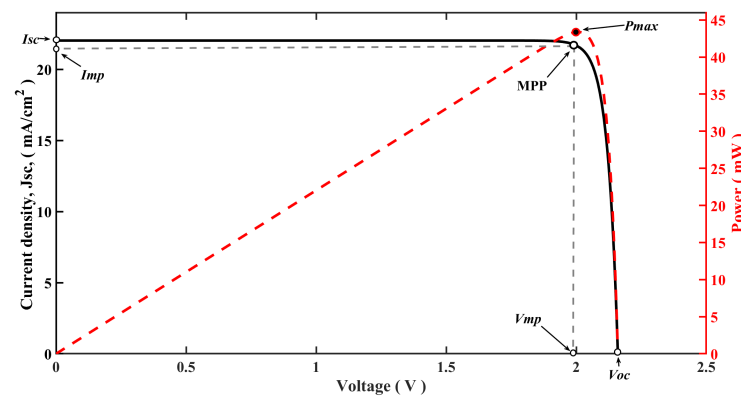
Figure 9. I-V and P-V characteristic curve of the perovskite-on-Si tandem solar cell used on this study.

4.3. Hybrid RF-Perovskite Energy Harvesting System

Hybrid RF-perovskite energy harvesting optimises efficiency and addresses constraints of standalone systems, enhancing reliability across environmental conditions, extending device lifespans, and advancing sustainability, especially in IoT and wireless sensor networks. The proposed system aims to provide a continuous power supply to IoT devices, enabling autonomous operation. The total energy harvested over 24 h by the hybrid system is the cumulative sum of the energy captured by individual components, as defined by (31).

$$E_{hybrid} = E_{RF} + E_{PSCs}. \tag{31}$$

Mathematically, for the proposed MIMO and array configurations, (31) is expanded below:

$$E_{hybrid} = \sum_{N=1}^{N=2^a} E_{RF_N} + \sum_{k=1}^{k=X_p} \left(P_{PSCs_k} \times t_{PSCs_k} \right). \tag{32}$$

Here, N represents the number of antennas in the MIMO system, expressed as 2^a (where a =1, 2, 3...), and k denotes the number of modules in an array. Equations (22) and (23) determine the energy harvested by the PSC array, taking into account the number of parallel modules, (Xp) (Figure 8).

The proposed RF-PSC energy harvester subsystems, connected in parallel, independently capture energy from RF signals and light irradiation, storing it in capacitor-based energy storage. This stored energy sustains IoT devices during low irradiation periods, such as at night when only RF-EH operates or in the daytime when PSCs and RF-EH face challenges due to low light or insufficient RF power. The hybrid system ensures uninterrupted power harvesting, even in subsystem failure or inadequate power generation, enhancing the overall efficiency. Mathematical determination, outlined in (33), considers the efficiencies of RF-EH, η_{RF}, and the array, η_A, derived from (9) and (30).

$$\eta_{hybrid} = 1 - \left[(1 - \eta_{RF}) \times (1 - \eta_A) \right]. \tag{33}$$

4.4. IoT Device Energy Consumption

IoT devices play a key role in data collection for environmental monitoring and security applications. Optimising their performance involves considering factors like individual voltage range, power needs, and energy consumption. Ensuring sufficient captured energy

is vital to sustain device operation and lifespan in energy harvesting systems. The total energy required by an IoT device (E_{IoT}) is expressed as follows:

$$E_{IoT} = P_{IoT} \times t_{IoT}. \tag{34}$$

P_{IoT} represents the power consumption of the IoT device, and t_{IoT} denotes its operation time. The operation time of the IoT device, t_{IoT}, considering multiple modes, such as sleep (t_s), standby (t_{sb}), power-off (t_{po}), power storing (t_{ps}), etc., can be obtained as follows:

$$t_{IoT} = \tau_o - (t_s + t_{sb} + t_{po} + t_{ps} + t_1 + t_2 + \ldots + t_n). \tag{35}$$

In (35), τ_o represents the maximum operation time (24 h) for the IoT device. t_1, t_2 and t_n are the duration of other power modes such as communication, processing, and other overpower modes. For a multi-mode active IoT device, the energy budget balance can be determined as follows:

$$E_{IoT} = E_s + E_{sb} + E_p + E_{ps} + E_1 + \ldots + E_n, \tag{36}$$

where E_s, E_{sb}, E_p, E_{ps}, and E_n represent the IoT energy during sleep mode at t_s, standby mode at t_{sb}, power-off mode at t_{po}, power-storing mode at t_{ps}, and other modes at t_n, respectively.

The hybrid RF-PSC system needs to produce energy from its surroundings consistently to ensure the continuous operation of IoT devices. Moreover, the generated energy must meet or surpass the power requirements of IoT devices, as shown in (37). The lifetime of an IoT device ($T_{lifetime}$) indicates its operational duration before ceasing to function, depending on its data gathering and measurement activities [56]. The formula used to calculate the network lifetime is expressed as (38).

$$E_{hybride} \geq E_{IoT}, \tag{37}$$

$$T_{lifetime} = \frac{(E_i - E_w)}{E_c + P_c \times R_p}. \tag{38}$$

In (38), E_i refers to the initial energy of the device, E_w is the wasted energy, E_c is the consumed energy, P_c is the overall power consumed, and R_p is the rate at which packets are received.

5. Results and Discussion

The rectifier, shown in Figure 6, was simulated over a range of input RF powers (-25 dBm to 20 dBm) to evaluate its performance regarding output voltage, efficiency, and power. As shown in Figures 10 and 11, both output voltage and efficiency at a 50 Ohm load increased consistently with rising RF input. Specifically, the output voltage started at 0.2 V at -5 dBm and peaked at 1.8 V at 20 dBm. Notably, meaningful output power and current were observed only for RF inputs exceeding 5 dBm, peaking at 27 mA and 45 mW at 20 dBm (Figures 10 and 11). However, the generated power remains insufficient for IoT devices, prompting the exploration of alternative architectures to enhance the rectifier's output capabilities. Additionally, Figure 11 illustrates that the rectifier achieves an efficiency of 20% at -5 dBm, increasing to a maximum of 52%.
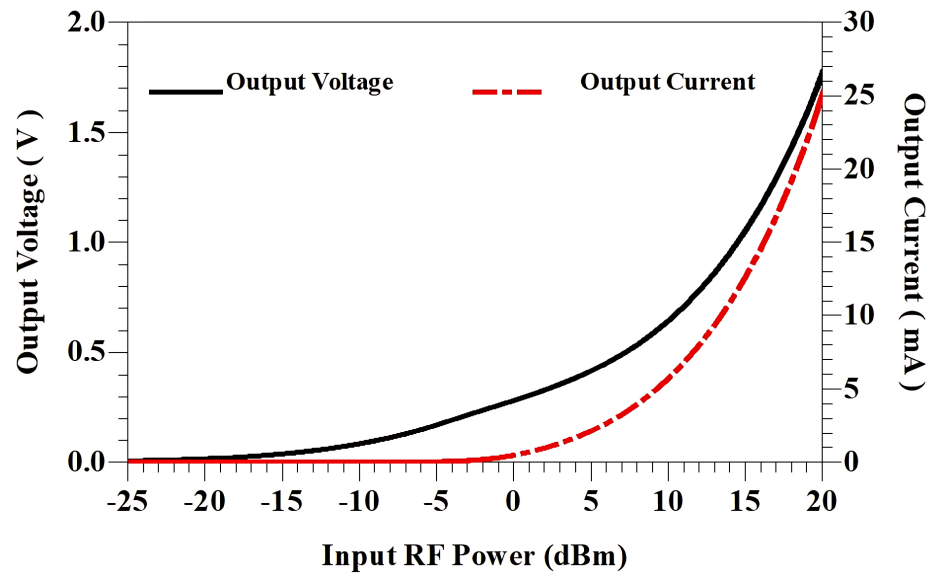
Figure 10. The proposed rectifier's output voltage measured at the node (Vdc), shown in Figure 6, and current at different input RF power levels.
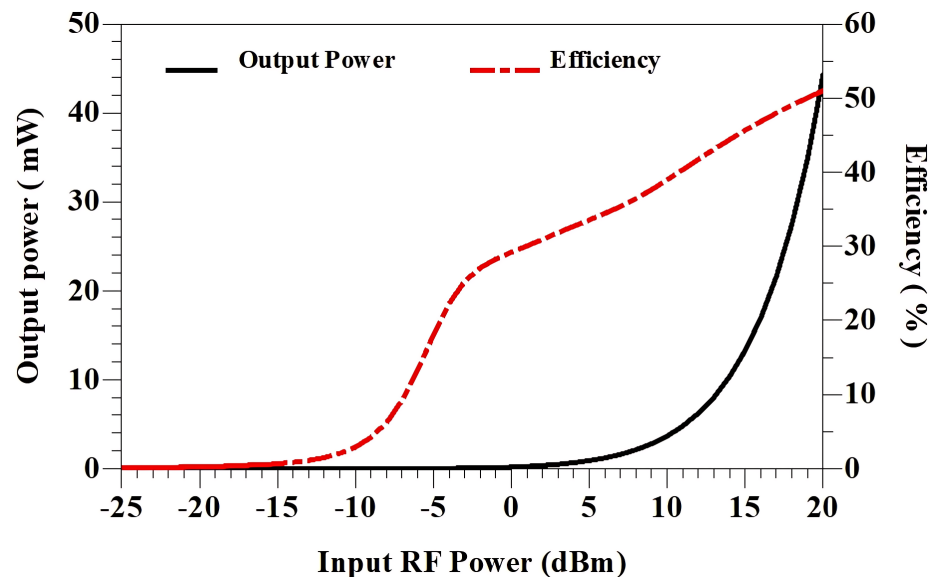

Figure 11. The rectifier's output power measured at the node (Vdc) (refer to Figure 6) and efficiency for different input RF power levels.

The RF-EH, single antenna, and rectifier were evaluated across a range of load resistances (50−1000 ohms) and input RF power levels (Figures 12 and 13). As load resistance increased, both efficiency and output voltage generally improved. At an input power of 20 dBm, the output voltage rose significantly for resistances up to 450 ohms, peaking at 6.5 V at 1 kohm. Meanwhile, the efficiency gradually increased with load resistance at all input RF power level values, reaching a maximum of 83% for 450 ohms and 20 dBm (Figure 13). For load resistances above 450 ohms at 20 dBm, efficiency declined because the output voltage increased only slightly compared to the increase in load resistance, while the input power remained constant.
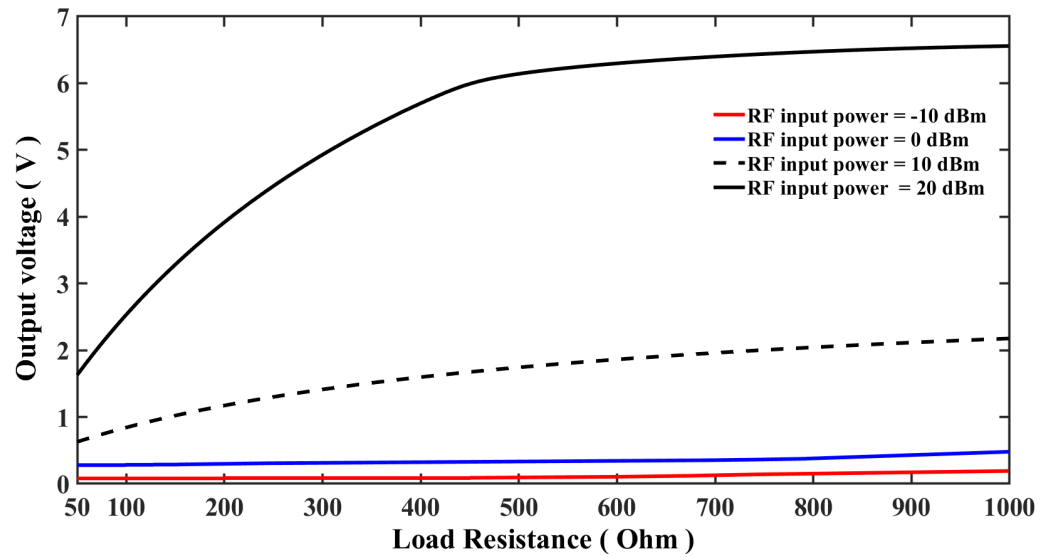
Figure 12. The output voltage of a single–antenna RF energy harvester across various loads and diverse levels of RF input power.
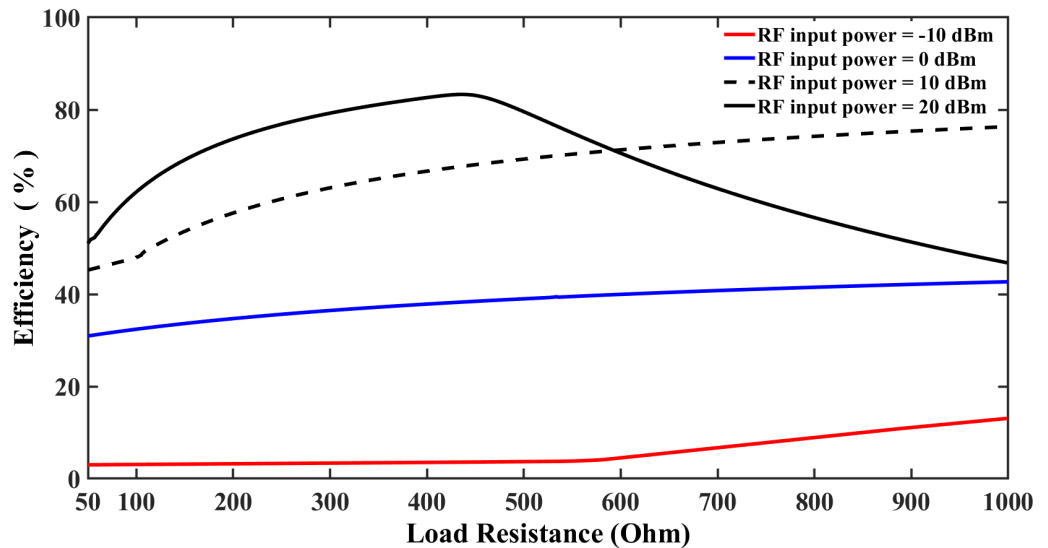
Figure 13. The efficiency of a single–antenna RF energy harvester under different loads and RF input power levels.

Various MIMO configurations, ranging from 2 to 16 antennas, were explored to enhance power output for IoT devices. Simulation results (Figures 14–16) demonstrate a steady increase in output voltage, current, and power as the number of antennas increases. Figure 14 shows that MIMO systems can generate output voltage even at −10 dBm input power; practical voltage is achieved only at higher RF input levels. At 20 dBm, the maximum voltages recorded are 6.3 V, 4.5 V, 3.2 V, 2.4 V, and 1.8 V for MIMO configurations with 16, 8, 4, 2, and 1 antennas. Notably, all MIMO setups at low RF input exhibit reduced output, highlighting inadequacy for IoT power requirements. This is due to power dissipation across rectifier diodes, a challenge mitigated by employing diodes with low voltage drop or utilising cascade rectifiers.
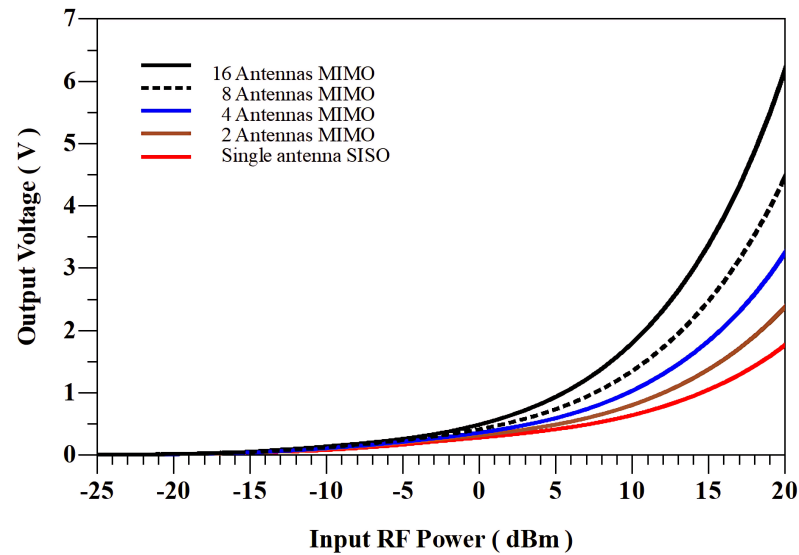
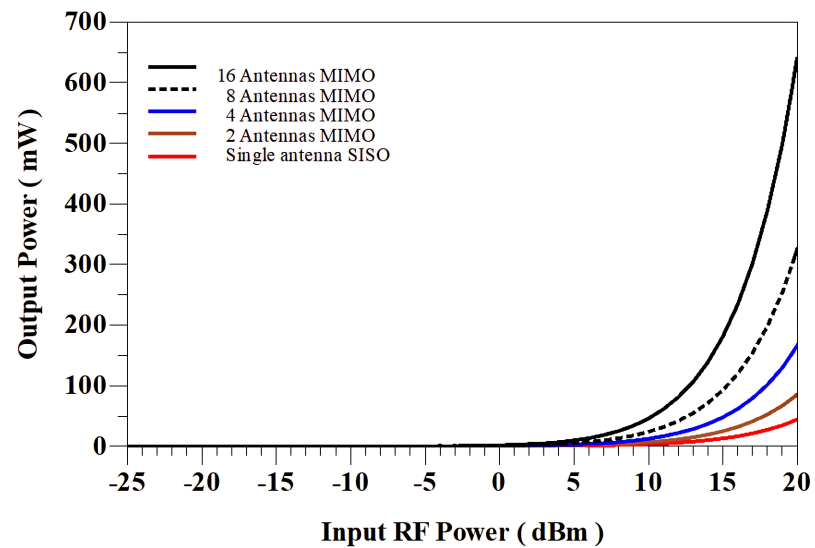**Figure 14.** The MIMO RF-EH output voltage at various RF input power levels.

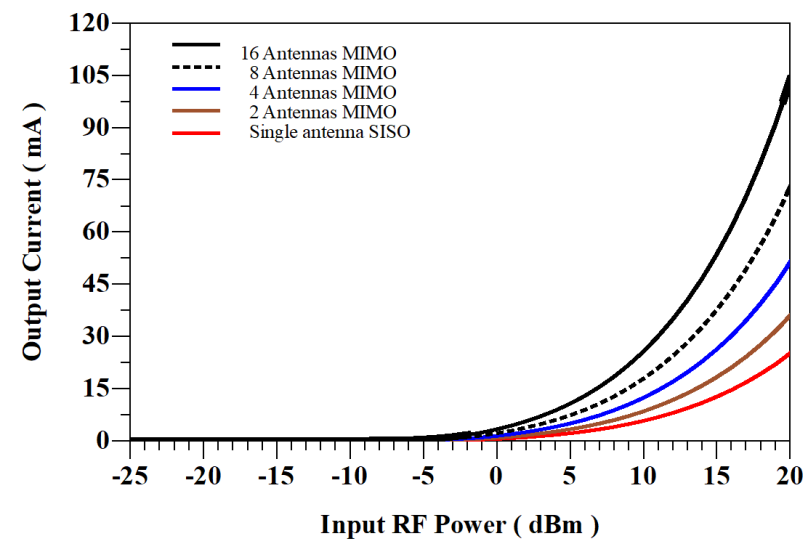**Figure 15.** The output power of the MIMO RF-EH at different RF input power.

Figure 16. The MIMO RF-EH output current at varying input RF power levels.

The MIMO designs' efficiency is assessed using (5) and (9). Figure 17 depicts the system's efficiency, indicating a notable rise in the growing antenna count. Efficiency exceeds 95% at higher input power levels, showcasing the system's effectiveness. Moreover, it underscores that increasing the number of antennas improves efficiency for low inputs. The output voltage, current, and power of the 16-antenna MIMO RF-EH, as depicted in Figures 14–16, peak at 6.1 V, 108 mA, and 649 mW. This highlights the system's ability to power IoT devices under high RF input conditions. However, alternative energy sources are necessary for low RF input scenarios.
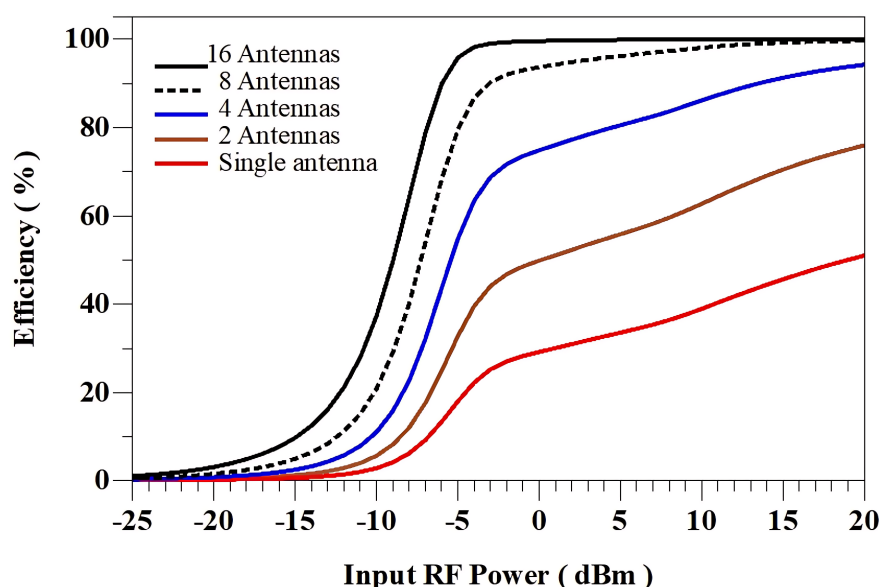
Figure 17. Efficiency of the MIMO of RF-EH at different levels of input RF power.

The I-V and P-V simulation results conducted in ADS and MATLAB are depicted in Figure 18 and Figure 8, respectively. From the simulations, I_{mp}, V_{mp}, and P_{max} were obtained at 21.69 mA, 1.99 V, and 43.36 mW. Additionally, V_{oc} of 2.2 V and I_{sc} of 23 mA are shown.

Figure 18. I-V and P-V characteristic curve of the perovskite-on-Si tandem solar cell with ADS-based simulation.

An array of five modules, each comprising three cells, was designed to enhance output power, achieving a P_{max} of 650 mW at 6.1 V and 108 mA. MATLAB-based (Figure 19) and ADS-based (Figure 20) simulations illustrate V_{oc} of 6.4 V and I_{sc} of 110 mA. Assuming an irradiation of 1000 W/m², the cell's efficiency is 48%; therefore, using (28), the efficiency of each module is found to be 11% and for the array is calculated as 44% using (30).
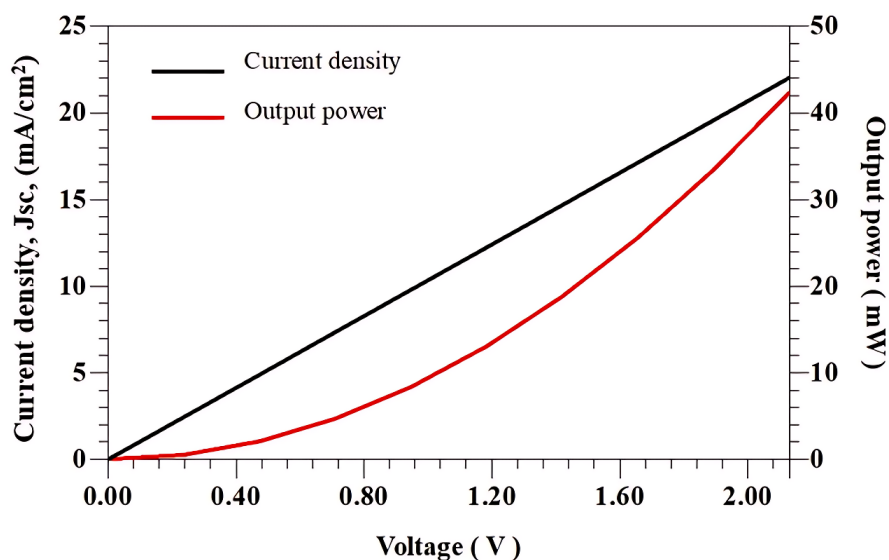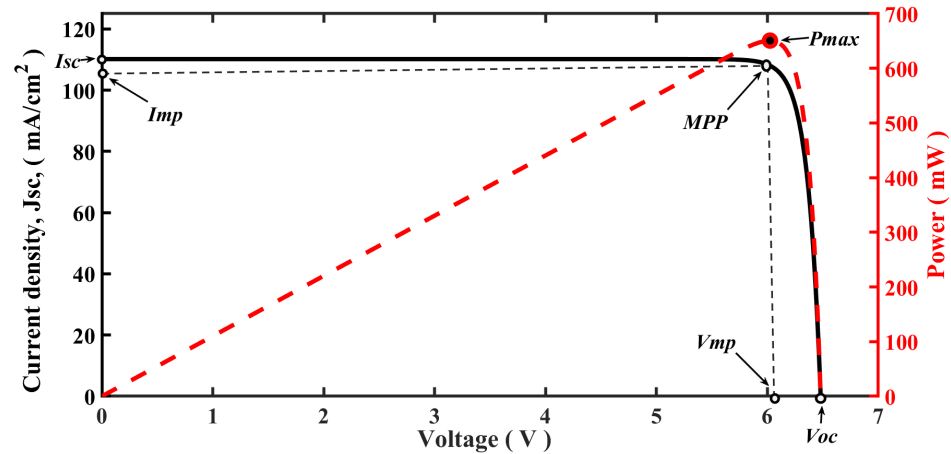

Figure 19. I-V and P-V characteristic curve of the perovskite-on-Si tandem solar array with MATLAB simulation.
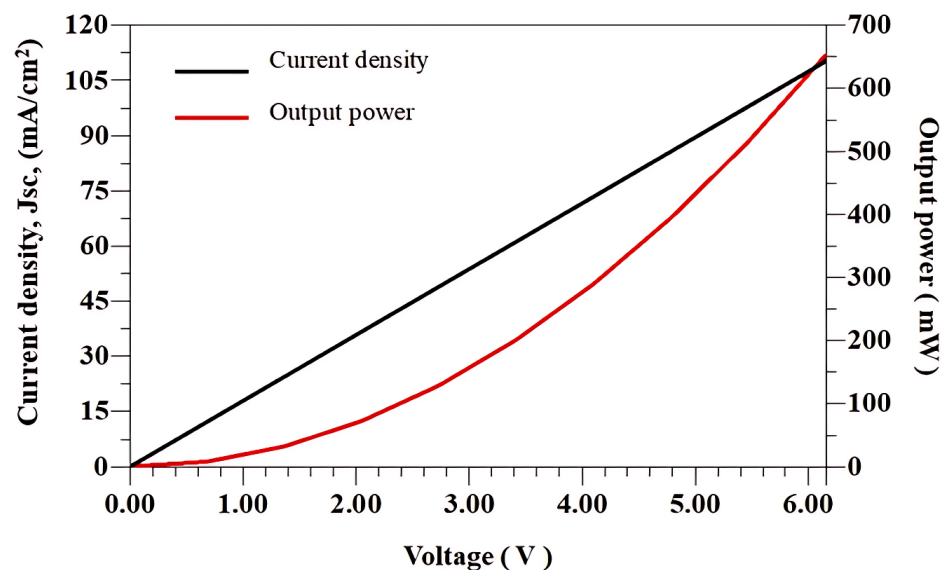
Figure 20. I-V and P-V characteristic curve of the perovskite-on-Si tandem solar array with ADS-based simulation.

The integration of MIMO RF and solar energy harvesting is crucial due to their complementary nature. This ensures continuous power availability for IoT applications under varying environmental conditions. While perovskite solar cells provide high-efficiency energy conversion during sunlight hours, RF energy harvesting remains effective even in low-light scenarios, such as cloudy or rainy days. This dual-source approach significantly enhances system reliability and minimises power interruptions.

Figure 21 showcases the hybrid energy harvester's performance, merging a MIMO setup with a PSCs array, predominantly during daylight when the perovskite cells reach peak output. It indicates the hybrid system's capability to produce significant power during the day, powering IoT devices and storing surplus energy in a storage unit, particularly with the 16 MIMO configuration. During low-light conditions, only the RF subsystem of the hybrid operates, generating lower power. Nevertheless, the excess energy stored

during high-light periods can be utilised. Since both subsystems function concurrently, the hybrid system's efficiency can be computed using (33), accounting for the efficiencies of both the array and RF-EH. Hence, the hybrid energy harvester attains an efficiency of 90%.

One of the primary challenges in using both sources simultaneously is efficiency optimisation. Perovskite solar cells can generate sufficient power during peak sunlight, potentially overshadowing RF harvesting. However, in scenarios where solar energy is unavailable, such as during night-time or heavy cloud cover, RF energy harvesting can sustain IoT devices [49]. To address efficiency concerns, an intelligent power management unit (PMU) will be incorporated to dynamically regulate power distribution, prioritising solar energy when available and switching to RF energy when solar input is insufficient. This hybrid approach allows for continuous and resilient energy harvesting in diverse environments, making it a viable solution for large-scale IoT deployments.
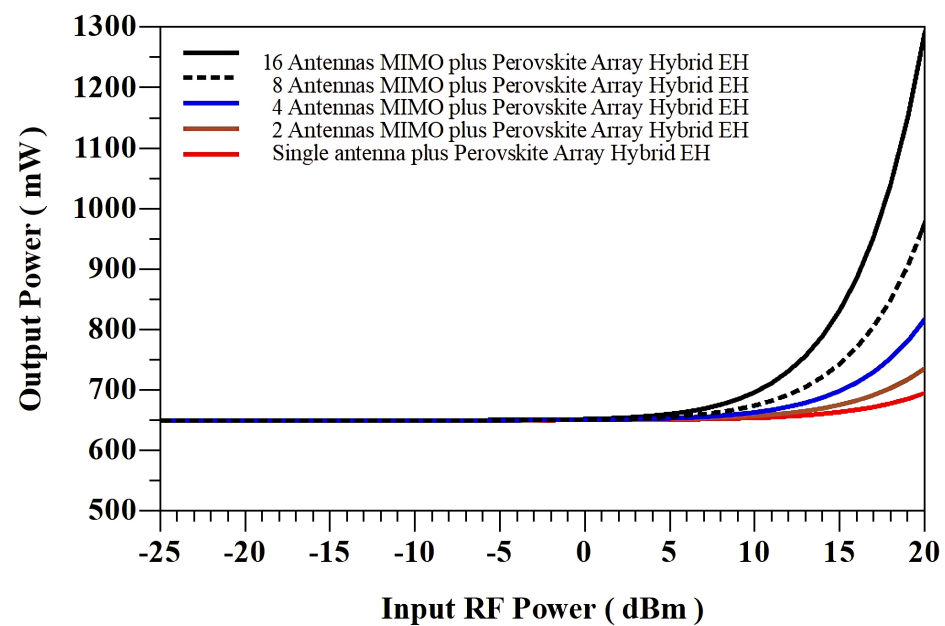
Figure 21. The power output of hybrid RF-PSC configurations varies across different levels of RF input power, particularly at the peak power point of the PSC array under irradiation of 1000 W/m².

Evaluating the impact of environmental factors is crucial for ensuring the efficiency and stability of the hybrid RF-PPV energy harvester when moving from simulation-based analysis to real-world deployment. While simulations provide valuable insights into theoretical performance, practical implementation must account for variables such as temperature fluctuations, humidity-induced degradation, and RF signal attenuation due to atmospheric conditions. A detailed investigation of temperature effects on perovskite photovoltaic cells was evaluated in [57–59], focusing on the power conversion efficiency and degradation mechanisms at varying temperatures. PSCs exhibit strong thermal stability between 20 °C and 55 °C, with a low power temperature coefficient of -0.25% °C^{-1}, outperforming $c - Si$ solar cells [59]. In the practical aspect of this study, advanced encapsulation techniques will be employed to protect perovskite materials from thermal stress (for temperature > 55 °C) and prolong operational stability. High humidity levels can also accelerate perovskite degradation, reducing efficiency over time [60]. Hence, protective coatings and encapsulation methods are proposed to improve resistance to moisture-related deterioration.

In terms of RF propagation, atmospheric conditions such as rain and fog introduce signal attenuation, necessitating frequency diversity. Adaptive filtering techniques will be used to optimise energy reception under varying environmental conditions. Moreover, multiple RF sources in smart city environments introduce potential interference, which will be addressed through strategies such as frequency diversity, spread-spectrum techniques, and adaptive filtering. Long-term system stability will be examined, including material degradation rates and performance retention over extended deployment periods.

5.1. Comparative Analysis of Hybrid RF-PSC Energy Harvesting with Other Technologies

The feasibility and advantages of the proposed hybrid RF-PSC energy harvesting system must be evaluated. Hence, a comparative assessment of the proposed hybrid RF-PSC system against alternative energy harvesting technologies has been incorporated. Thermoelectric energy harvesting (TEG) systems, which convert waste heat into electricity, offer a viable solution in industrial applications but are constrained by their lower power density than RF-PSC hybrids [61]. Vibrational energy harvesters, including piezoelectric and electromagnetic systems, have also been explored. While effective in converting mechanical vibrations into energy, these systems require frequent movement, limiting their suitability for static IoT applications. A comprehensive comparison table summarising these systems' power density, efficiency, scalability, and deployment costs is provided in Table 1.

Table 1. Comparison of energy harvesting technologies.

Technology	Power Density	Efficiency	Scalability	Reference
RF-PSC Hybrid	11 μW–110 μW/cm^2–Combining RF and Perovskite	>90%	Excellent	This paper
Thermoelectric (TEG)	40 μW–10 mW/cm^3–Industrial 1 μW–60 μW/cm^3—Wearable	10–50%	Good	[62–64]
Piezoelectric	0.33 mW–30 mW/cm^3	25–50%	Good	[62,65–67]
Electromagnetic	4 μW–306 μW/cm^3	60–70%	Moderate	[62,63]
Perovskite-PV	10 μW–100 μW/cm^2	20–38%	Excellent	[45,55,62,68]
Solar (PV) Outdoor	15mW/cm^3—Sunny day 0.15 mW/cm^3—Cloudy day	10–25%	Excellent	[33,62,63,69]
RF Energy	0.08 nW–6.3 μW/cm^2	30–88%	Good	[69–71]

5.2. Cost–Benefit Analysis and Scalability of Hybrid RF-PSC Energy Harvesting Systems

The financial viability of energy harvesting technologies is crucial for widespread adoption, particularly in cost-sensitive applications such as large-scale IoT networks. Hybrid RF-PSC systems offer a promising alternative to conventional battery-powered and standalone solar solutions by enhancing energy efficiency and reducing long-term operational costs. The cost of materials, including perovskite solar cells and RF antennas, has been compared against conventional battery-powered and standalone solar solutions. Installation and maintenance costs have been assessed, focusing on deployment scalability, PSC longevity encapsulation methods, and RF antenna recalibration requirements. The analysis also highlights the economic benefits of reducing battery dependency, particularly in large-scale IoT networks. The cost analysis is provided in Table 2.

Table 2. Cost–benefit comparison of hybrid RF-PSC and conventional systems.

Category	Hybrid RF-PSC System	Conventional Systems (Solar Panels/Battery-Powered IoT)	Remarks/Notes
Material Costs	Moderate, USD 50 to USD 80 per unit (PSC + RF antenna) [72–76]	High, USD 70 to USD 100 per solar panel USD 10 to USD 20 per battery [72,77,78]	PSCs are cheaper than silicon PV cells; batteries require frequent replacement. MIMO RF antennas add moderate cost.
Installation Costs	Moderate, USD 30 to USD 50 per device [72,76,76]	Moderate–High, USD 50 to USD 80 per device [72,77]	Hybrid systems require integration of RF and PSCs with IoT devices; solar panels need structural support and batteries require distributed installations.
Maintenance Costs (annually)	Low–Moderate, USD 5 to USD 10 per device [72,73,76]	High, USD 20 to USD 30 per device [72,77]	PSCs require encapsulation to extend lifespan; batteries need frequent replacement; solar panels require cleaning and periodic inspection.
Battery Dependency	Minimal, USD 5 to USD 10 annually [46]	High, USD 10 to USD 15 per battery annually [79]	Hybrid systems reduce battery dependency significantly, lowering long-term costs and environmental impact.
Lifespan	20–25 years (with encapsulation) [72,75,80,81]	5–7 years for batteries 10–15 years for panels [79,81]	PSC lifespan depends on encapsulation; batteries degrade faster.

In a large-scale IoT deployment of 1000 devices over 10 years, the hybrid RF-PSC system demonstrates a significantly lower total cost, which is a reduction of approximately 50% compared to conventional solar and battery-powered systems. It benefits from reduced material, installation, and maintenance expenses and minimal battery dependency. This leads to substantial cost savings over time, with a shorter return-on-investment period (3–5 years due to reduced maintenance and battery replacement costs) and enhanced economic viability for large-scale IoT networks [73,81]. An RF-PSC hybrid system offers linear scalability with minimal additional costs, unlike conventional battery-powered systems, which face exponential scaling challenges due to logistical constraints. Thus, the RF-PSC hybrid system provides a financially feasible and operationally efficient alternative. Its scalability and efficiency make it well-suited for sustainable and cost-effective IoT deployments, ensuring long-term reliability with reduced maintenance and energy costs.

6. Conclusions

To solve the inadequate output voltage caused by low input RF power, the single-antenna RF-EH was altered to incorporate an MIMO system with multiple antennas, significantly improving voltage and efficiency. The MIMO RF-EH achieved a 95% efficiency with a peak output voltage of 6.3 V, although voltage fluctuated with RF signal strength. Despite this, the MIMO system provides key insights for developing hybrid RF-perovskite energy harvesters for low-power IoT applications. Integrating RF-EH and perovskite photovoltaic technologies holds promise for achieving sustainable and self-sufficient IoT systems, leveraging their complementary strengths and overcoming individual limitations. The study's mathematical modelling tools provide a novel approach to examining system architecture and identifying the compatibility of perovskite solar and RF-EH systems. This study demonstrates that increasing MIMO configurations can generate sufficient power, particularly at high input RF power levels (>10 dBm). However, due to the intermittent nature of high RF power, the study proposes a significant solution: integrating PSCs as an alternative energy source. This approach enhances the reliability and autonomy of IoT devices, ensuring continuous operation even during low RF input power periods. By combining MIMO RF-EH and PSC technologies, this research offers a solution that is not

only cost-effective and high-performing but also flexible, allowing for low-temperature processing and prolonged operation without frequent battery replacements.

This research offers innovative solutions for smart cities, providing sustainable power for sensors and IoT devices to enhance urban infrastructure and operations. The hybrid RF-perovskite energy harvester can be integrated into buildings, creating smarter, energy-efficient spaces while enabling wirelessly charged health-monitoring sensors in homes and public areas. The technology can also contribute to a smart economy by optimising energy use, monitoring consumption, and reducing reliance on non-renewable sources. In remote agricultural areas and critical infrastructure, it powers IoT devices for monitoring soil, crop health, and structural integrity, improving sustainability and resilience. By combining MIMO RF-EH and PSCs technologies, this research delivers a versatile, cost-effective solution for diverse applications in smart cities and remote settings. It enhances IoT device reliability and autonomy, ensuring uninterrupted operation and establishing hybrid energy harvesting as a key enabler of future smart cities.

While simulation results highlight the potential of integrating MIMO RF-EH with perovskite photovoltaics to enhance energy efficiency and device autonomy, real-world testing is essential to validate its practical performance and adaptability in dynamic environments. Acknowledging the importance of real-world validation, we have outlined a future experimental plan to assess the system's practical performance. The prototype will be tested in urban environments, analysing its functionality under diverse indoor and outdoor conditions. Key performance indicators, such as energy yield variations, efficiency under dynamic RF conditions, and IoT device uptime, will be measured over extended deployment periods. Encapsulation technique and protective coatings will be employed in the practical aspect of this study to protect perovskite materials and prolong operational stability. Furthermore, we plan to integrate the system with IoT networks and evaluate its communication reliability and energy sustainability in smart city infrastructures. The impact of environmental stressors, user mobility, and network congestion will be analysed to refine system robustness. These future studies will strengthen the real-world applicability of hybrid RF-PSC energy harvesting technologies.

References

1. Balsamo, D.; Magno, M.; Kubara, K.; Lazarescu, B.; Merrett, G.V. Energy Harvesting Meets IoT: Fuelling Adoption of Transient Computing in Embedded Systems. In Proceedings of the 2019 IEEE 5th World Forum on Internet of Things (WF-IoT), Limerick, Ireland, 15–18 April 2019; pp. 413–417. [CrossRef]
2. Villa-Ávila, E.; Arévalo, P.; Ochoa-Correa, D.; Villa-Ávila, M.; Sempértegui-Moscoso, E.; Jurado, F. A New Methodology for Estimating the Potential for Photovoltaic Electricity Generation on Urban Building Rooftops for Self-Consumption Applications. *Smart Cities* **2024**, *7*, 3798–3822. [CrossRef]
3. Al-Rimawi, T.; Nadler, M. Leveraging Smart City Technologies for Enhanced Real Estate Development: An Integrative Review. *Smart Cities* **2025**, *8*, 10. [CrossRef]
4. Souzandeh, N.; Dashti Ardakani, M.; Aïssa, S.; Ovidiu Tatu, S. Frequency Selective CMOS RF-to-DC Rectifier for Wireless Power and RFID Applications. In Proceedings of the 2020 International Symposium on Networks, Computers and Communications (ISNCC), Montreal, QC, Canada, 20–22 October 2020; pp. 1–6. [CrossRef]
5. Elgarhy, O.; Reggiani, L.; Malik, H.; Alam, M.M.; Imran, M.A. Rate-Latency Optimization for NB-IoT with Adaptive Resource Unit Configuration in Uplink Transmission. *IEEE Syst. J.* **2021**, *15*, 265–276. [CrossRef]
6. Lorincz, J.; Klarin, Z. A Comprehensive Analysis of the Impact of an Increase in User Devices on the Long-Term Energy Efficiency of 5G Networks. *Smart Cities* **2024**, *7*, 3616–3657. [CrossRef]
7. Jeena, G.; Uko, M.; Ekpo, S.; Elias, F. Design of an elliptically-slotted patch antenna for multi-purpose wireless wi-fi and biosensing applications. *e-Prime Adv. Electr. Eng. Electron. Energy* **2023**, *6*, 100368. [CrossRef]
8. Zafar, M.; Ekpo, S.; George, J.; Sheedy, P.; Uko, M.; Gibson, A. Hybrid power divider and combiner for passive RFID tag wireless energy harvesting. *IEEE Access* **2021**, *10*, 502–515. [CrossRef]
9. Lau, I.; Ekpo, S.; Zafar, M.; Ijaz, M.; Gibson, A. Hybrid mmWave-Li-Fi 5G Architecture for Reconfigurable Variable Latency and Data Rate Communications. *IEEE Access* **2023**, *11*, 42850–42861. [CrossRef]
10. ENAHORO, S.; Ekpo, S.; Uko, M.; Alabi, S.; Elias, F.; Unnikrishnan, R. A Metamaterial-Grounded Ultra-Wideband Cross-Fractal MIMO Antenna for K, Ka, and mmWave Applications. *e-Prime Adv. Electr. Eng. Electron. Energy* **2023**, 1–19. [CrossRef]
11. Ekpo, S.C. Parametric system engineering analysis of capability-based small satellite missions. *IEEE Syst. J.* **2019**, *13*, 3546–3555. [CrossRef]
12. Ekpo, S.C. Thermal subsystem operational times analysis for ubiquitous small satellites relay in LEO. *Int. Rev. Aerosp. Eng. (IREASE)* **2018**, *11*, 48–57. [CrossRef]
13. Ekpo, S.C.; Adebisi, B.; Wells, A. Regulated-element frost beamformer for vehicular multimedia sound enhancement and noise reduction applications. *IEEE Access* **2017**, *5*, 27254–27262. [CrossRef]
14. Uko, M.; Ekpo, S. A 23–28 GHz pHEMT MMIC Low-Noise Amplifier for Satellite-Cellular Convergence Applications. *Int. Rev. Aerosp. Eng. J.* **2021**, *14*, 1–10. [CrossRef]
15. Ekpo, S.C.; Adebisi, B.; George, D.; Kharel, R.; Uko, M. System-level multicriteria modelling of payload operational times for communication satellite missions in LEO. *Recent Prog. Space Technol.* **2014**, *4*, 67–77.
16. Ekpo, S.C.; George, D. Reconfigurable cooperative intelligent control design for space missions. *Recent Patents Space Technol.* **2012**, *2*, 2–11. [CrossRef]
17. Uko, M.; Ekpo, S.C.; Enahoro, S.; Elias, F. Performance Optimization of 5G–Satellite Integrated Networks for IoT Applications in Smart Cities: A Two-Ray Propagation Model Approach. *Smart Cities* **2024**, *7*, 3895–3913. [CrossRef]
18. Uko, M.; Ekpo, S.; Elias, F.; Alabi, S. A 3.2–3.8 GHz low-noise amplifier for 5G/6G satellite-cellular convergence applications. *e-Prime Adv. Electr. Eng. Electron. Energy* **2024**, *8*, 100559. [CrossRef]
19. Kim, S.; Vyas, R.; Bito, J.; Niotaki, K.; Collado, A.; Georgiadis, A.; Tentzeris, M.M. Ambient RF Energy-Harvesting Technologies for Self-Sustainable Standalone Wireless Sensor Platforms. *Proc. IEEE* **2014**, *102*, 1649–1666. [CrossRef]
20. Ekpo, S.C.; George, D. A power budget model for highly adaptive small satellites. *Recent Patents Space Technol.* **2013**, *3*, 118–127.
21. Jung, J.; Kwon, I. A capacitive dc-dc boost converter with gate bias boosting and dynamic body biasing for an rf energy harvesting system. *Sensors* **2022**, *23*, 395. [CrossRef]
22. Uko, M.; Elias, F.; Ekpo, S.; Saha, D.; Ghosh, S.; Ijaz, M.; Chakraborty, S.; Gibson, A. Hybrid Wireless RF-Perovskite Photovoltaic Energy Harvester Design Consideration for Low-Power Internet of Things. In Proceedings of the 2023 IEEE-APS Topical Conference on Antennas and Propagation in Wireless Communications (APWC), Venice, Italy, 9–13 October 2023; pp. 173–176. [CrossRef]
23. Kim, H.; Kwon, I. Design of high-efficiency CMOS rectifier with low reverse leakage for RF energy harvesting. *Electron. Lett.* **2019**, *55*, 446–448. [CrossRef]
24. Sowande, O.; Idachaba, F.; Ekpo, S.; Faruk, N.; Uko, M.; Ogunmodimu, O. Sub-6 GHz 5G Spectrum for Satellite-Cellular Convergence Broadband Internet Access in Nigeria. *Int. Rev. Aerosp. Eng.* **2022**, *15*, 85–96. [CrossRef]
25. Sleppy, J.; Silverstein, A.; Moser, D. Unlocking the Future with Flexible, Wire-Shaped Supercapacitors. *J. Fluid Flow* **2021**, *8*, 238–243. [CrossRef]

26. Elabany, A.; Nassar, A.; Mostafa, H. Design Optimization of Multi-Input Reconfigurable Capacitive DC-DC Converters: A CAD Tool Approach. In Proceedings of the 2021 IEEE International Symposium on Circuits and Systems (ISCAS), Daegu, Republic of Korea, 22–28 May 2021; pp. 1–5. [CrossRef]

27. Ghosh, S.; Chakraborty, S.; Saha, D.; Ekpo, S.C.; Chakraborty, A.; Elias, F.; Uko, M. Design and Analysis of mm-Wave MIMO SIW Antenna for Multibeam 5G Applications. In Proceedings of the 2023 IEEE-APS Topical Conference on Antennas and Propagation in Wireless Communications (APWC), Venice, Italy, 9–13 October 2023; pp. 154–159. [CrossRef]

28. Khan, T.A.; Yazdan, A.; Heath, R.W. Optimization of Power Transfer Efficiency and Energy Efficiency for Wireless-Powered Systems with Massive MIMO. *IEEE Trans. Wirel. Commun.* **2018**, *17*, 7159–7172. [CrossRef]

29. Ippili, S.; Jella, V.; Eom, S.; Hong, S.; Yoon, S.G. Light-driven piezo-and triboelectricity in organic–inorganic metal trihalide perovskite toward mechanical energy harvesting and self-powered sensor application. *ACS Appl. Mater. Interfaces* **2020**, *12*, 50472–50483. [CrossRef]

30. Cui, T.; Li, J.; Shen, J.; Dong, S. Performance Analysis for MIMO SWIPT Systems with Space-Time Coding. In *IOP Conference Series: Materials Science and Engineering, Proceedings of the 3rd International Conference on Aerospace Technology, Communications and Energy Systems (ATCES 2019), Nanjing, China, 26–29 September 2019*; IOP Publishing: Bristol, UK, 2019; Volume 685, p. 012027.

31. Li, S.; Wan, Z.; Jin, L.; Du, J. Energy harvesting maximizing for millimeter-wave massive MIMO-NOMA. *Electronics* **2019**, *9*, 32. [CrossRef]

32. Jeong, Y.; Shin, D.; Park, J.H.; Park, J.; Yi, Y.; Im, S. Integrated advantages from perovskite photovoltaic cell and 2D MoTe2 transistor towards self-power energy harvesting and photosensing. *Nano Energy* **2019**, *63*, 103833. [CrossRef]

33. Nishimura, S.; Watahiki, T.; Niinobe, D.; Hayashida, T.; Yuda, Y.; Kano, S.; Nishimura, K.; Tokioka, H.; Yamamuka, M. Over 21% Efficiency of n-Type Monocrystalline Silicon PERT Photovoltaic Cell with Boron Emitter. *IEEE J. Photovoltaics* **2016**, *6*, 846–851. [CrossRef]

34. Rohatgi, A.; Zhu, K.; Tong, J.; Kim, D.H.; Reichmanis, E.; Rounsaville, B.; Prakash, V.; Ok, Y.W. 26.7% Efficient 4-Terminal Perovskite–Silicon Tandem Solar Cell Composed of a High-Performance Semitransparent Perovskite Cell and a Doped Poly-Si/SiOx Passivating Contact Silicon Cell. *IEEE J. Photovoltaics* **2020**, *10*, 417–422. [CrossRef]

35. Cariou, R.; Benick, J.; Feldmann, F.; Höhn, O.; Hauser, H.; Beutel, P.; Razek, N.; Wimplinger, M.; Bläsi, B.; Lackner, D.; et al. III–V-on-silicon solar cells reaching 33% photoconversion efficiency in two-terminal configuration. *Nat. Energy* **2018**, *3*, 326–333. [CrossRef]

36. Essig, S.; Allebé, C.; Remo, T.; Geisz, J.F.; Steiner, M.A.; Horowitz, K.; Barraud, L.; Ward, J.S.; Schnabel, M.; Descoeudres, A.; et al. Raising the one-sun conversion efficiency of III–V/Si solar cells to 32.8% for two junctions and 35.9% for three junctions. *Nat. Energy* **2017**, *2*, 17144. [CrossRef]

37. Mahapatra, A.; Prochowicz, D.; Tavakoli, M.M.; Trivedi, S.; Kumar, P.; Yadav, P. A review of aspects of additive engineering in perovskite solar cells. *J. Mater. Chem. A* **2020**, *8*, 27–54. [CrossRef]

38. Davis, M.A.; Sweat, R.; Yu, Z. Predictive Modeling of Cracking Behaviors in Flexible Perovskite Solar Cells. *IEEE J. Flex. Electron.* **2022**, *1*, 231–235. [CrossRef]

39. Mathews, I.; Kantareddy, S.N.R.; Sun, S.; Layurova, M.; Thapa, J.; Correa-Baena, J.P.; Bhattacharyya, R.; Buonassisi, T.; Sarma, S.; Peters, I.M. Self-powered sensors enabled by wide-bandgap perovskite indoor photovoltaic cells. *Adv. Funct. Mater.* **2019**, *29*, 1904072. [CrossRef]

40. Hu, Z.; Lin, Z.; Su, J.; Zhang, J.; Chang, J.; Hao, Y. A Review on Energy Band-Gap Engineering for Perovskite Photovoltaics. *Solar RRL* **2019**, *3*, 1900304. [CrossRef]

41. Xiao, Y.; Lestrade, M.; Li, Z.; Li, Z.S. Modeling of Perovskite/Si Tandem Solar Cell. In Proceedings of the 2023 IEEE 50th Photovoltaic Specialists Conference (PVSC), San Juan, PR, USA, 11–16 June 2023; pp. 1–3. [CrossRef]

42. He, F.; Fei, W.; Wang, Y.; Liu, C.; Guo, Q.; Lan, W.; Fan, G.; Lu, G.; Chen, D.; Zhu, W.; et al. Wide-Bandgap All-Inorganic CsPbIBr2 Top Cells with MoOx/Ag/TeO2 Composite Transparent Anode Towards Efficient Four-Terminal Perovskite/Si Tandem Solar Cells. *IEEE Photonics J.* **2021**, *13*, 8400108. [CrossRef]

43. Bush, K.A.; Bailie, C.D.; Chen, Y.; Bowring, A.R.; Wang, W.; Ma, W.; Leijtens, T.; Moghadam, F.; McGehee, M.D. Thermal and environmental stability of semi-transparent perovskite solar cells for tandems enabled by a solution-processed nanoparticle buffer layer and sputtered ITO electrode. *Adv. Mater.* **2016**, *28*, 3937–3943. [CrossRef]

44. Tong, J.; Song, Z.; Kim, D.H.; Chen, X.; Chen, C.; Palmstrom, A.F.; Ndione, P.F.; Reese, M.O.; Dunfield, S.P.; Reid, O.G.; et al. Carrier lifetimes of >1 µs in Sn-Pb perovskites enable efficient all-perovskite tandem solar cells. *Science* **2019**, *364*, 475–479. [CrossRef]

45. Gburi, A.M.A.A.; Drăgulinescu, A. Perovskite and CIGS Solar Cells for Energy Harvesting: Design, Simulation and Comparison. In Proceedings of the 2023 International Semiconductor Conference (CAS), Sinaia, Romania, 11–13 October 2023; pp. 193–196. [CrossRef]

46. Kantareddy, S.N.R.; Mathews, I.; Sun, S.; Layurova, M.; Thapa, J.; Correa-Baena, J.P.; Bhattacharyya, R.; Buonassisi, T.; Sarma, S.E.; Peters, I.M. Perovskite PV-Powered RFID: Enabling Low-Cost Self-Powered IoT Sensors. *IEEE Sens. J.* **2020**, *20*, 471–478. [CrossRef]

47. Elias, F.; Ekpo, S.; Alabi, S.; Saha, D.; Chakraborty, S.; Ghosh, S.; Uko, M.; Ijaz, M.; Umar, R. Rectifier and Reconfigurable Impedance Matching Network Analysis for Wireless Sub-6 GHz 5G/Wi-Fi 6/6E Energy Harvester. In Proceedings of the Second International Adaptive and Sustainable Science, Engineering and Technology ASSET Conference, Manchster, UK, 18–20 July 2023; Springer: Cham, Switzerland, 2024; pp. 81–90.

48. Xu, Z.; Khalifa, A.; Mittal, A.; Nasrollahpourmotlaghzanjani, M.; Etienne-Cummings, R.; Xiang Sun, N.; Cash, S.S.; Shrivastava, A. Analysis and Design Methodology of RF Energy Harvesting Rectifier Circuit for Ultra-Low Power Applications. *IEEE Open J. Circuits Syst.* **2022**, *3*, 82–96. [CrossRef]

49. Elias, F.; Ekpo, S.; Alabi, S.; Enahoro, S.; Uko, M.; Ijaz, M.; Ji, H.; Unnikrishnan, R.; Olasunkanmi, N. Passive Massive MIMO Hybrid RF-Perovskite Energy Harvesting Frontend for LEO Satellite Applications. In Proceedings of the 5th Space Passive Component Days (SPCD 2024), European Space Agency (ESA), ESA/ESTEC, Noordwijk, The Netherlands, 15–18 October 2024; pp. 1–7.

50. Lu, X.; Wang, P.; Niyato, D.; Kim, D.I.; Han, Z. Wireless Networks with RF Energy Harvesting: A Contemporary Survey. *IEEE Commun. Surv. Tutorials* **2015**, *17*, 757–789. [CrossRef]

51. Al-Ashouri, A.; Köhnen, E.; Li, B.; Magomedov, A.; Hempel, H.; Caprioglio, P.; Márquez, J.A.; Morales Vilches, A.B.; Kasparavicius, E.; Smith, J.A.; et al. Monolithic perovskite/silicon tandem solar cell with >29% efficiency by enhanced hole extraction. *Science* **2020**, *370*, 1300–1309. [CrossRef]

52. Kim, J.Y.; Lee, J.W.; Jung, H.S.; Shin, H.; Park, N.G. High-efficiency perovskite solar cells. *Chem. Rev.* **2020**, *120*, 7867–7918. [CrossRef]

53. Hoarcă, I.C. Mathematical modeling and simulation of PV systems Part I: Mathematical modeling and Simulink implementation. In Proceedings of the 2021 International Conference on Applied and Theoretical Electricity (ICATE), Craiova, Romania, 27–29 May 2021; pp. 1–6. [CrossRef]

54. Vinod; Kumar, R.; Singh, S. Solar photovoltaic modeling and simulation: As a renewable energy solution. *Energy Rep.* **2018**, *4*, 701–712. [CrossRef]

55. Kumar, S.G.; N, S.; Pramod, A.; R, P.C.; Honnavar, G.V. Investigating the Performance of a Wide Bandgap BaZrS3 Perovskite Tandem Solar Cell. In Proceedings of the 2023 International Conference on Smart Systems for applications in Electrical Sciences (ICSSES), Tumakuru, India, 7–8 July 2023; pp. 1–6. [CrossRef]

56. Rabah, S.; Zaier, A.; Lloret, J.; Dahman, H. Efficiency Enhancement of a Hybrid Sustainable Energy Harvesting System Using HHHOPSO-MPPT for IoT Devices. *Sustainability* **2023**, *15*, 10252. [CrossRef]

57. Halal, A.; Alnahhal, A.I.; Plesz, B. Performance Analysis of Perovskite Solar Cell by Considering Temperature Effect on Physical Parameters of the Absorber Layer. In Proceedings of the 2022 28th International Workshop on Thermal Investigations of ICs and Systems (THERMINIC), Dublin, Ireland, 28–30 September 2022; pp. 1–4. [CrossRef]

58. Mortadi, A.; Tabbai, Y.; Hafidi, E.E.; Nasrellah, H.; Chahid, E.; Monkade, M.; Moznine, R.E. Investigating temperature effects on perovskite solar cell performance via SCAPS-1D and impedance spectroscopy. *Clean. Eng. Technol.* **2025**, *24*, 100876. [CrossRef]

59. Halal, A.; Plesz, B. A Comprehensive Study on the Thermal Behavior of Perovskite Solar Cell. *IEEE Trans. Components Packag. Manuf.* **2024**, *14*, 1753–1760. [CrossRef]

60. Mishra, A.K.; Shukla, R. Effect of humidity in the perovskite solar cell. *Mater. Today Proc.* **2020**, *29*, 836–838. [CrossRef]

61. Veloo, S.G.; Tiang, J.J.; Muhammad, S.; Wong, S.K. A Hybrid Solar-RF Energy Harvesting System Based on an EM4325-Embedded RFID Tag. *Electronics* **2023**, *12*, 4045. [CrossRef]

62. Sherazi, H.H.R.; Zorbas, D.; O'Flynn, B. A Comprehensive Survey on RF Energy Harvesting: Applications and Performance Determinants. *Sensors* **2022**, *22*, 2990. [CrossRef] [PubMed]

63. Pozo, B.; Garate, J.I.; Araujo, J.A.; Ferreiro, S. Energy Harvesting Technologies and Equivalent Electronic Structural Models—Review. *Electronics* **2019**, *8*, 486. [CrossRef]

64. Lenz, C.; Vostrikov, S.; Mayer, P.; Magno, M. From Heat to Power: Assessing Thermoelectric Energy Harvesting for Self-sustainable Sensors. In Proceedings of the 2023 IEEE International Workshop on Technologies for Defense and Security (TechDefense), Rome, Italy, 20–22 November 2023; pp. 384–389. [CrossRef]

65. Azmi, M.Z.; Adnan, S.F.S. Energy Generating from Footsteps on Piezoelectric Module. In Proceedings of the 2024 IEEE Industrial Electronics and Applications Conference (IEACon), Kuala Lumpur, Malaysia, 4–5 November 2024; pp. 152–156. [CrossRef]

66. Ghazanfarian, J.; Mohammadi, M.M.; Uchino, K. Piezoelectric Energy Harvesting: A Systematic Review of Reviews. *Actuators* **2021**, *10*, 312. [CrossRef]

67. Covaci, C.; Gontean, A. Piezoelectric Energy Harvesting Solutions: A Review. *Sensors* **2020**, *20*, 3512. [CrossRef]

68. Olzhabay, Y.; Ng, A.; Ukaegbu, I.A. Perovskite PV Energy Harvesting System for Uninterrupted IoT Device Applications. *Energies* **2021**, *14*, 7946. [CrossRef]

69. Tang, X.; Wang, X.; Cattley, R.; Gu, F.; Ball, A.D. Energy Harvesting Technologies for Achieving Self-Powered Wireless Sensor Networks in Machine Condition Monitoring: A Review. *Sensors* **2018**, *18*, 4113. [CrossRef] [PubMed]

70. Saeed, W.; Shoaib, N.; Cheema, H.M.; Khan, M.U. RF energy harvesting for ubiquitous, zero power wireless sensors. *Int. J. Antennas Propag.* **2018**, *2018*, 8903139. [CrossRef]

71. Pinuela, M.; Mitcheson, P.D.; Lucyszyn, S. Ambient RF energy harvesting in urban and semi-urban environments. *IEEE Trans. Microw. Theory Tech.* **2013**, *61*, 2715–2726. [CrossRef]

72. Zafoschnig, L.A.; Nold, S.; Goldschmidt, J.C. The Race for Lowest Costs of Electricity Production: Techno-Economic Analysis of Silicon, Perovskite and Tandem Solar Cells. *IEEE J. Photovoltaics* **2020**, *10*, 1632–1641. [CrossRef]

73. Čulík, P.; Brooks, K.; Momblona, C.; Adams, M.; Kinge, S.; Maréchal, F.; Dyson, P.J.; Nazeeruddin, M.K. Design and Cost Analysis of 100 MW Perovskite Solar Panel Manufacturing Process in Different Locations. *ACS Energy Lett.* **2022**, *7*, 3039–3044. [CrossRef]

74. Zhang, C.; Park, N.G. Materials and Methods for Cost-Effective Fabrication of Perovskite Photovoltaic Devices. *Commun. Mater.* **2024**, *5*, 194. [CrossRef]

75. Li, G.; Chen, H. Manufacturing Cost Analysis of Single-Junction Perovskite Solar Cells. *Solar RRL* **2024**, *8*, 2400540. [CrossRef]

76. Kajal, P.; Verma, B.; Vadaga, S.G.R.; Powar, S. Costing Analysis of Scalable Carbon-Based Perovskite Modules Using Bottom-Up Technique. *Glob. Challenges* **2022**, *6*, 2100070. [CrossRef]

77. Ramasamy, V.; Zuboy, J.; Woodhouse, M.; O'Shaughnessy, E.; Feldman, D.; Desai, J.; Walker, A.; Margolis, R.; Basore, P. *U.S. Solar Photovoltaic System and Energy Storage Cost Benchmarks, with Minimum Sustainable Price Analysis: Q1 2023*; Technical Report NREL/TP-7A40-87303; National Renewable Energy Laboratory (NREL), U.S. Department of Energy: Golden, CO, USA, 2023.

78. U.S. Department of Energy, Solar Energy Technologies Office. *Solar Photovoltaic System Cost Benchmarks*; Technical Report; U.S. Department of Energy (DOE) Solar Energy Technologies Office (SETO): Washington, DC, USA, 2023.

79. Prauzek, M.; Konecny, J.; Borova, M.; Janosova, K.; Hlavica, J.; Musilek, P. Energy Harvesting Sources, Storage Devices and System Topologies for Environmental Wireless Sensor Networks: A Review. *Sensors* **2018**, *18*, 2446. [CrossRef]

80. Tian, X.; Stranks, S.D.; You, F. Life Cycle Energy Use and Environmental Implications of High-Performance Perovskite Tandem Solar Cells. *Sci. Adv.* **2020**, *6*, eabb0055. [CrossRef] [PubMed]

81. Benstead, M.; He, X. *Perovskite Photovoltaic Market 2025–2035: Technologies, Players and Trends*; Technical Report; IDTechEx: Boston, MA, USA, 2025.